An Exploration of All-Inorganic Perovskite/Gallium Arsenide Tandem Solar Cells

Jiaping Wang, Peng Zhao, Ying Hu, Zhenhua Lin,* Jie Su, Jincheng Zhang, Jingjing Chang,* and Yue Hao

All-inorganic perovskite/gallium arsenide (GaAs) tandem solar cells are of great interest for potential space applications. Herein, planar all-inorganic four-terminal (4-T) and two-terminal (2-T) perovskite/GaAs tandem solar cells are simulated and optimized, respectively. To achieve higher absorption in the 4-T configuration, the reflection and parasitic absorption have to be reduced through optimizing the thickness of the perovskite and GaAs base, reducing the thickness of SnO_2 and the organic hole transport layer (HTL), and introducing an antireflection coating, respectively. To balance the short-circuit current and open-circuit voltage of the GaAs bottom cell, the doping concentration on GaAs is optimized to $10^{18}\,cm^{-3}$ that has resulted in a high power conversion efficiency (PCE) of 30.97%. Based on the results of 4-T configuration, all-inorganic perovskites with different halide compositions are used for current matching to achieve a high-efficiency 2-T configuration. After studying the effects of defect density and optimizing the doping concentration of the GaAs base, an extremely high PCE of 30.67% is achieved based on 2-T $CsPbIBr_2$/GaAs tandem solar cells. Furthermore, the current mismatching under the AM0 spectrum is eliminated for potential high altitude/space application, and the device offers a very competitive PCE of 27.23% compared with that of traditional GaAs double-junction tandem solar cells.

1. Introduction

In recent years, with the intensive studies by a large number of researchers, great progresses have been made in perovskite solar cells (PSCs). The power conversion efficiency (PCE) has improved from 3.7%[1] to 25.5%,[2–4] whereas the device performances were

J. Wang, P. Zhao, Y. Hu, Dr. Z. Lin, Dr. J. Su, Prof. J. Zhang, Prof. J. Chang, Prof. Y. Hao
State Key Discipline Laboratory of Wide Band Gap Semiconductor Technology
Shaanxi Joint Key Laboratory of Graphene
School of Microelectronics
Xidian University
2 South Taibai Road, Xi'an 710071, China
E-mail: zhlin@xidian.edu.cn; jjingchang@xidian.edu.cn

Prof. J. Zhang, Prof. J. Chang, Prof. Y. Hao
Advanced Interdisciplinary Research Center for Flexible Electronics
Xidian University
2 South Taibai Road, Xi'an 710071, China

The ORCID identification number(s) for the author(s) of this article can be found under https://doi.org/10.1002/solr.202100121.

less than 5% degradation under continuous illumination for more than 1800 h at 70–75 °C.[5] In addition, perovskite materials have many advantages, including great photoelectric performance, long carrier diffusion lengths, tunable bandgap, and low manufacturing costs.[6–11]

However, PSCs are less efficient than traditional crystalline silicon-based solar cells, and all solar cells are limited by the Shockley–Queisser (S–Q) limit.[12] Compared with traditional single-junction PSCs, a double-junction solar cell is composed of two subcell modules and can break the S–Q limit and further extend PCE.[13] The top cell of a double-junction solar cell has a wider bandgap and can absorb shorter wavelengths of solar spectrum to reduce thermalization of excess energy loss. Correspondingly, the bottom cell has a smaller bandgap and is able to capture photons with lower energy in long wavelengths of the solar spectrum, which could not be absorbed by a wide band semiconductor. Tandem solar cells can be divided into two-terminal (2-T) and four-terminal (4-T) devices. Among them, the 4-T device is composed of two independent subcells. After the shortwave solar spectrum is partially absorbed by the top cell, the remaining part is injected into the bottom cell and then captured. Meantime, a transparent conductive glass is utilized as the back electrode of the top cell to minimize photon transmission loss. This structure ensures that the processes of the subcells, including high-temperature annealing and additional antireflection coating (ARC), can be carried through. The 2-T device is monolithic and has two subcells connected by an intermediate tunneling layer or a recombination layer. This monolithic configuration with an intermediate layer facilitates carrier transport and can save raw materials. However, the overall current of the 2-T cells is limited by one of the subcells with smaller current. So, for 2-T tandem solar cells, current matching is a guarantee of the excellent efficiency.[14]

There are reports of perovskite tandem solar cells that PSCs were selected as top cell, whereas copper indium gallium selenide (CIGS) solar cells, crystalline silicon solar cells, organic solar cells, or PSCs are as a bottom cell.[15–20] The device of a highest PCE of 29.2% composed of PSCs and crystalline silicon solar cells.[4,21] As the 2-T perovskite tandem solar cell was first

reported by Mailoa et al.,[22] researchers have continuously improved the fabrication process of perovskite tandem solar cells through the hybrid deposition, blade coated, and other methods.[23,24] By introducing advanced recombination layer and front top metal grid design, the PCE of large-area perovskite tandem solar cells has progressed unceasingly.[25,26] In summary, perovskite tandem solar cells are considered to have great potential as one of the most promising commercial solutions for PSCs.

Recently, Cardinaletti et al.[27] reported the possibility of a space application of PSCs and confirmed their stability to a certain degree. However, conventional organic–inorganic hybrid PSCs contain organic cations, such as MA^+ and FA^+, which could be easily decomposed by heat, therefore limiting their applications in space. Due to better thermal stability of all-inorganic perovskites,[28] new opportunities are opened up for PSCs to produce energy efficiently and stably in space. Park and co-workers[29] reported the perovskite/gallium arsenide (GaAs) tandem device with the PCE of 24.27% for 2-T configuration and 25.19% for 4-T configuration. Compared with traditional GaAs double-junction solar cells, perovskite/GaAs tandem solar cells have lower fabrication costs and simpler tunnel junctions. Although this investigation of perovskite/GaAs double-junction solar cells has made some progress, it still has a gap with the ideal double-junction solar cell performance. According to Kurtz's models,[30] a top cell with a bandgap of 1.90–2.10 eV is ideal for a double-junction tandem solar cell, which includes GaAs bottom cell. In addition, the bandgap of all inorganic perovskite $CsPbI_{3-x}Br_x$ $(3 \geq x \geq 0)$ can be adjusted between 1.7 and 2.30 eV.[28] To further optimize the performance of GaAs double-junction solar cells, theoretical analysis and research of all-inorganic perovskite/GaAs tandem solar cells are performed. In our work, 2-T and 4-T all-inorganic perovskite/GaAs tandem solar cells are investigated. To reduce reflection and parasitic losses, thicknesses of perovskite, carrier transport layers, and GaAs base are optimized. To achieve better PCE, ARC is introduced, and front indium tin oxide (ITO) electrode is studied first. Then, the current matching is performed to obtain the optimal all-inorganic perovskite material; the doping concentration of GaAs base is optimized, and a high PCE of 30.67% is achieved

for 2-T $CsPbIBr_2$/GaAs tandem solar cells. Finally, an organic-free 2-T configuration is investigated by introducing NiO as a hole transport layer (HTL), and the high PCEs of 29.42% under AM1.5G and 27.23% under AM0 are achieved by eliminating current mismatching.

2. Results and Discussion

2.1. Simulation Results and Optimization of 4-T Configuration

2.1.1. Thickness of Absorber in Subcells

In the simulation of 4-T all-inorganic perovskite/GaAs tandem solar cells, $CsPbI_2Br$ is chosen as all-inorganic perovskite in the top cell due to its suitable bandgap and high PCE as an independent subcell.[30–34] As shown in **Figure 1**a, the SnO_2 electron transport layer (ETL) and organic HTL are used as parts of the high-performance inorganic PSCs. As the electrical and optical parameters of organic HTLs, such as poly[bis(4-phenyl)(2,4,6-trimethylphenyl)amine] (PTAA), 2,2′,7,7′-Tetra(N,N-di-p-tolyl) amino-9,9-spirobifluorene (spiro-TTB), and 2,2′,7,7′-Tetrakis[N,N-di-(4-methoxyphenyl)amino]-9,9′-spirobifluorene (spiro-OMeTAD), are similar, this study takes spiro-OMeTAD as an example.[24,34–36] To explore the performance characteristics of perovskite/GaAs solar cells and economize materials as much as possible, the first step is to determine the optimal thicknesses of the absorbing layers in the top cell and bottom cell. The parameters of the $CsPbI_2Br$ top cell and GaAs bottom cell in the simulation are summarized in **Table 1** and **2**, respectively. The refractive index n and extinction coefficient k of all-inorganic perovskites are calculated from the first-principle calculations[37] (Figure S1, Supporting Information) to ensure that the optical parameters of each material are obtained based on the same method, because the optical parameters show diversity from the literature.[38–42] All first-principle calculations are used by density functional theory with the projector augmented wave (PAW) method as implemented in the Vienna Ab-initio Simulation Package (VASP) code. Generalized gradient approximation (GGA) with Perdew–Burke–Emzerhof (PBE) functional
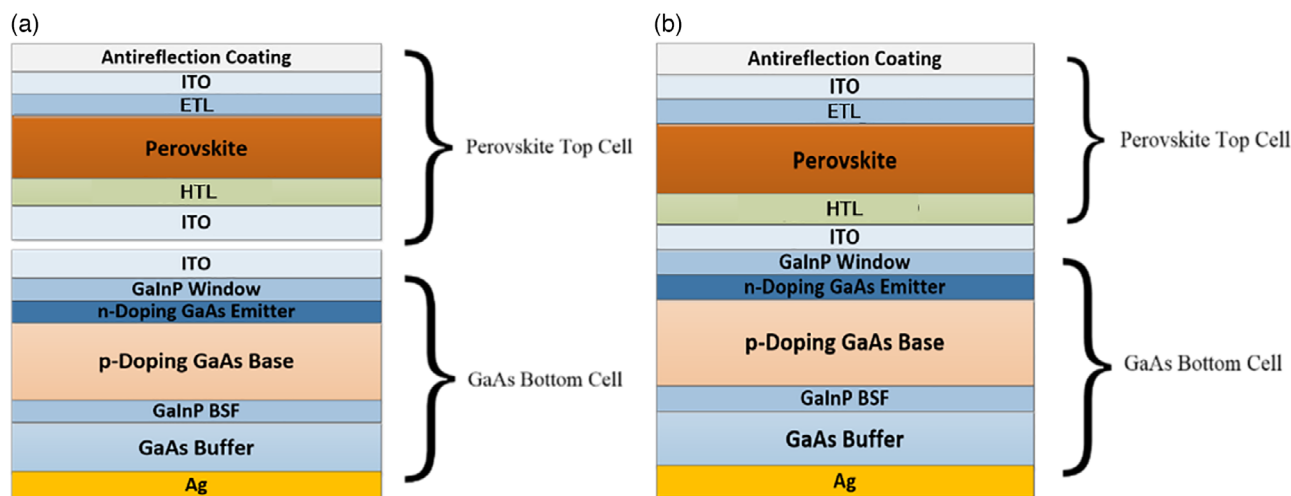
Figure 1. Configuration schematics of a) 4-T and b) 2-T perovskite/GaAs tandem solar cells.

Table 1. Parameters of CsPbI$_2$Br top cell.

	SnO$_2$	CsPbI$_2$Br	Spiro-OMeTAD
Accept density, N_A [cm^{-3}]	–	10^{15}	10^{20}
Donor density, N_D [cm^{-3}]	10^{20}	–	–
Bandgap energy, E_g [eV]	3.6[35]	1.82[53]	3.0[54]
Electron affinity, χ [eV]	4.4[35]	3.76[53]	2.45[54]
Relative dielectric permittivity, ε_r	9[35]	7.43[37]	3[54]
Effective conduction band density, N_c [cm^{-3}]	4.36 × 10$^{18[35]}$	5.1 × 10$^{17[37]}$	2.5 × 10$^{20[54]}$
Effective valence band density, N_v [cm^{-3}]	2.52 × 10$^{19[35]}$	1.8 × 10$^{18[37]}$	2.5 × 10$^{20[54]}$
Mobility of electron, μ_n [cm^2 (V s)$^{-1}$]	240[35]	1.02 × 10$^{5[37]}$	2 × 10$^{-4[35]}$
Mobility of hole, μ_p [cm^2 (V s)$^{-1}$]	25[35]	1.93 × 10$^{4[37]}$	2 × 10$^{-4[35]}$
Lifetime of electron, τ_n [s]	2.83 × 10$^{-2[35]}$	1.6 × 10$^{-8[37]}$	10$^{-7[35]}$
Lifetime of hole, τ_p [s]	2.83 × 10$^{-2[35]}$	1.6 × 10$^{-8[37]}$	10$^{-7[35]}$

Table 2. Parameters of GaAs bottom cell.

	GaAs	GaInP
Accept density, N_A [cm^{-3}]	10^{16} (base)	3 × 10^{17} (BSF)
Donor density, N_D [cm^{-3}]	10^{19} (emitter)	10^{18} (window)
Bandgap energy, E_g [eV]	1.42[43]	1.61[43]
Electron affinity, χ [eV]	4.07[43]	4.4[43]
Relative dielectric permittivity, ε_r	13.2[43]	12.1[43]
Effective conduction band density, N_c [cm^{-3}]	4.35 × 10$^{17[43]}$	7.18 × 10$^{17[43]}$
Effective valence band density, N_v [cm^{-3}]	8.16 × 10$^{18[43]}$	8.87 × 10$^{18[43]}$
Mobility of electron, μ_n [cm^2 (V s)$^{-1}$]	8000[43]	4600[43]
Mobility of hole, μ_p [cm^2 (V s)$^{-1}$]	400[43]	150[43]
Lifetime of electron, τ_n [s]	1 × 10$^{-9[43]}$	1[43]
Lifetime of hole, τ_p [s]	2 × 10$^{-8[43]}$	1[43]

is used. The refractive index n and extinction coefficient k of GaAs and GaInP are obtained from the literature[43] (Figure S2, Supporting Information).

As shown in **Figure 2**a, set the thickness of GaAs base constant to 3.5 μm, and the thickness of the perovskite increases from 50 to 600 nm. As a result, total PCE and top cell PCE show a wavy upward trend; then, they are saturated and fluctuated in a small range. Simultaneously, bottom cell PCE shows a downward trend in volatility. To further investigate the cause of this phenomenon, short-circuit current density (J_{sc}) and external quantum efficiency (EQE) of both subcells are simulated. As shown in Figure 2c, the fluctuation trend of PCE mainly comes from J_{sc}. Therefore, two thickness ranges of 90–140 and 200–250 nm are investigated. Figure 2d shows that the main absorption spectrum range of the top cell is 300–700 nm, whereas the bottom cell is 500–850 nm. Compared with the EQE of 90 and 140 nm perovskite thickness, the EQE of the top cell at 600–700 nm is improved, as the thickness of the perovskite increases. Correspondingly, the EQE of the bottom cell at the overlap of absorption spectra of the two subcells decreases significantly. Simultaneously, the EQE of the bottom cell in the 700–850 nm wavelength range increases obviously, which illustrates that the perovskite at a thickness of 140 nm has less red and IR light reflection loss. Because the perovskite layer can hardly absorb incident light with a wavelength greater than 700 nm, and after the light completes multiple reflections inside the perovskite film, the light can reach the GaAs bottom cell. At a specific thickness of perovskite, it is easier to form optical interference between the reflected light and the incident light of neighboring units, resulting in higher power loss in this wavelength range. Conversely, short-wavelength light is absorbed within a very short distance into the perovskite without reflection. The short wavelength EQE of perovskite has almost no fluctuations. It leads to low J_{sc} and PCE in GaAs bottom cell at a perovskite thickness of 90 nm. Figure 2e shows the EQE of subcells with 200 and 250 nm thickness perovskites. Different

from Figure 2d, the EQE of the top cell tends to be saturated and does not increase with the thicker perovskite. Hence, to increase the total photon absorption, it is necessary to reduce the reflection loss of tandem solar cells by selecting the appropriate thickness of perovskite. In addition, the variation of open-circuit voltage (V_{oc}) under the different thicknesses of perovskite is studied, as shown in Figure S2a, Supporting Information. When the thickness of the perovskite increases, V_{oc} of perovskite top cell continues to decrease, whereas V_{oc} of GaAs bottom cell remains almost unchanged, which can be attributed to the slight decrease in the difference between electron quasi-Fermi level (E_{fn}) and hole quasi-Fermi level (E_{fp}) in PSC (Figure S3b, Supporting Information). As shown in Figure 2b, the thickness of CsPbI$_2$Br is kept constant to 250 nm, and the GaAs base increases from 0.5 to 5.0 μm. The bottom cell PCE and total PCE first increase with the thickness of GaAs base increasing from 0.5 to 2.5 μm and then almost reached saturation. In addition, the results show that the increase in GaAs base thickness has no effect on the top cell PCE. Therefore, 250 nm CsPbI$_2$Br and 2.5 μm GaAs base with the total PCE of 24.61% are fixed in this study.

2.1.2. Study of Parasitic Absorption

In addition to reflection loss, parasitic absorption loss is another important factor affecting the photon absorption of solar cells, especially for tandem solar cells. For a single-junction PSC, most of the parasitic absorption is generated by the top carrier transport layer. However, in a perovskite tandem solar cell, the bottom carrier transport layer of the top cell may capture the absorption spectrum of the bottom cell, resulting in more complex parasitic absorption losses.

As shown in **Figure 3**a–c, the refractive loss in the wavelength range of 700–800 nm keeps decline with the organic HTL thickness decrease from 150 to 50 nm. In addition, parasitic absorption at the 300–400 nm wavelength range keeps decreasing with SnO$_2$ thickness change from 200 to 20 nm (Figure 3d–g). As for GaInP, its absorption is cut off at a wavelength of 600 nm, and this part of the photons is almost entirely absorbed by SnO$_2$ and CsPbI$_2$Br before, so the parasitic absorption loss is negligible. Through this measure, the total PCE of the 4-T perovskite/GaAs tandem solar cells is significantly increased from 24.61% to 28.90%.
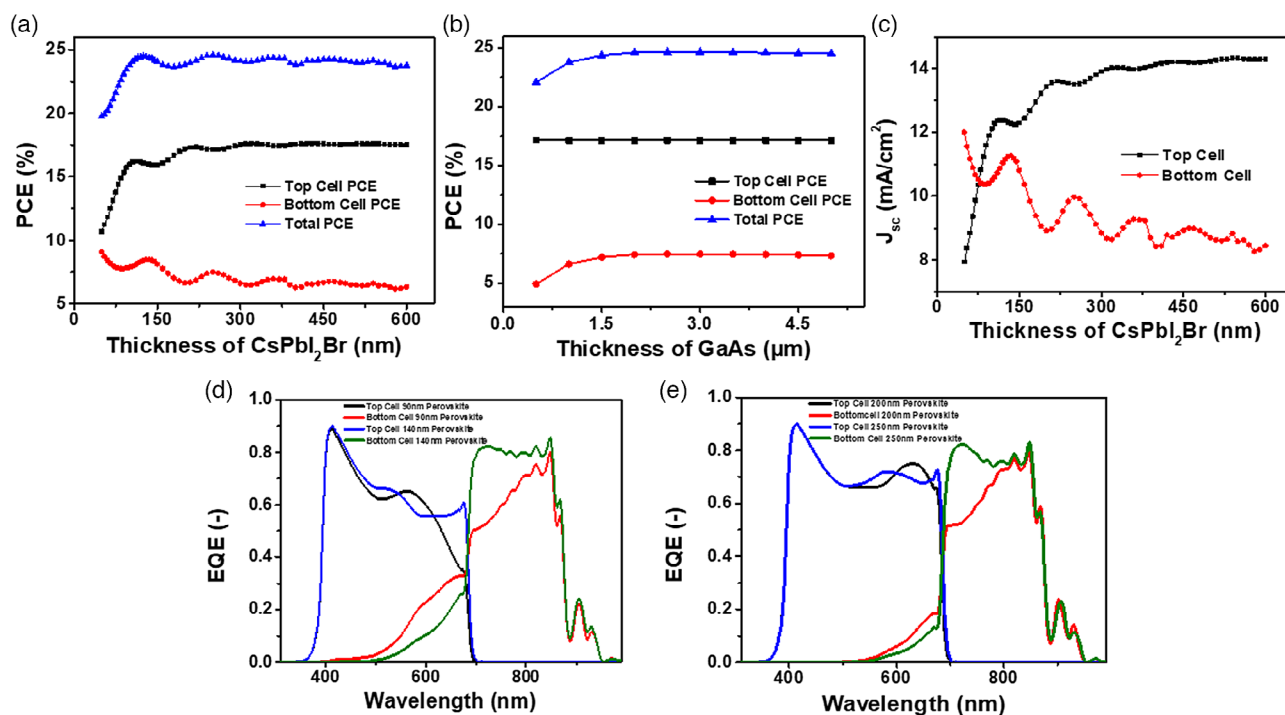
Figure 2. PCEs of 4-T CsPbI$_2$Br/GaAs tandem solar cells with different thicknesses of a) CsPbI$_2$Br (GaAs base: 3.5 µm) and b) GaAs base (CsPbI$_2$Br: 250 nm). c) J_{sc} of the subcells with different thicknesses of CsPbI$_2$Br. d) EQE spectra of the subcells with 90 and 140 nm perovskites. e) EQE spectra of the subcells with 200 and 250 nm perovskites.
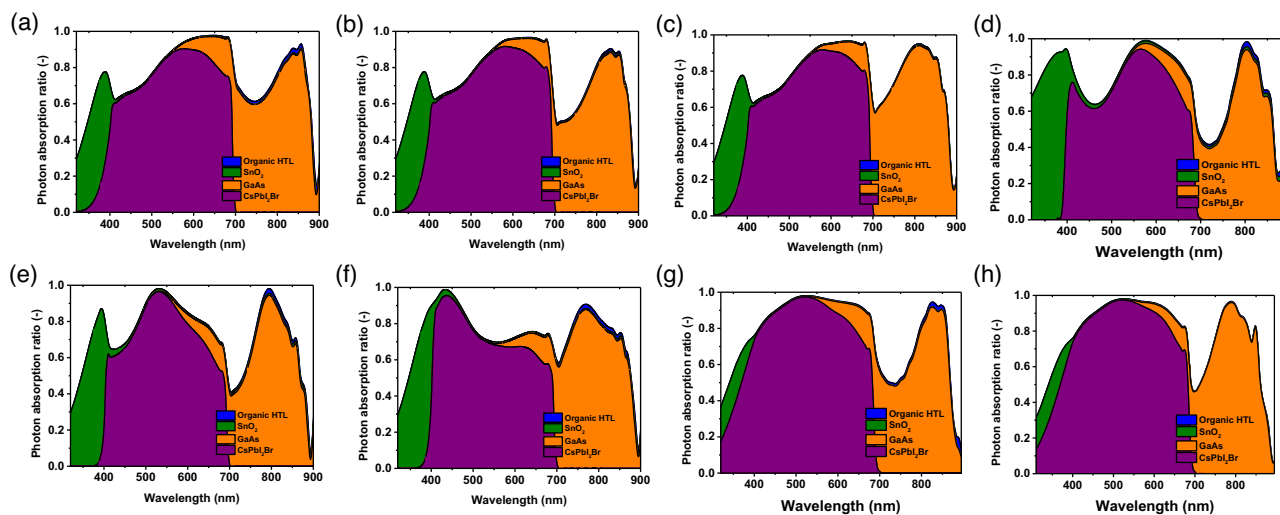

Figure 3. Absorption ratios of organic HTL, SnO$_2$, CsPbI$_2$Br, and GaAs in 4-T tandem solar cells with a) 50 nm SnO$_2$ and 150 nm organic HTL, b) 50 nm SnO$_2$ and 100 nm organic HTL, c) 50 nm SnO$_2$ and 50 nm organic HTL, d) 200 nm SnO$_2$ and 150 nm organic HTL, e) 150 nm SnO$_2$ and 150 nm organic HTL, f) 100 nm SnO$_2$ and 150 nm organic HTL, g) 20 nm SnO$_2$ and 150 nm organic HTL, and h) 20 nm SnO$_2$ and 50 nm organic HTL.

2.1.3. Study of ARC and Front ITO Electrode

To further improve the absorption of 4-T perovskite/GaAs tandem solar cells, it is necessary to provide a suitable ARC for the devices. We introduce LiF[29,44] with excellent antireflection performance in the study and place it on top of the tandem solar cells as ARC. As shown in **Figure 4**a, the total PCE increases to

some extent after the introduction of ARC. When the thickness of LiF increases, total PCE shows a trend of rising initially and then decreasing, reaching a maximum value at 50 nm. It is worth noting that as shown in Figure 4c, LiF is more sensitive to longer wavelength, which results in that as the thickness of LiF increases, the top cell PCE decreases, and the bottom cell PCE increases, as shown in Figure 4b. Meanwhile, Figure 4d
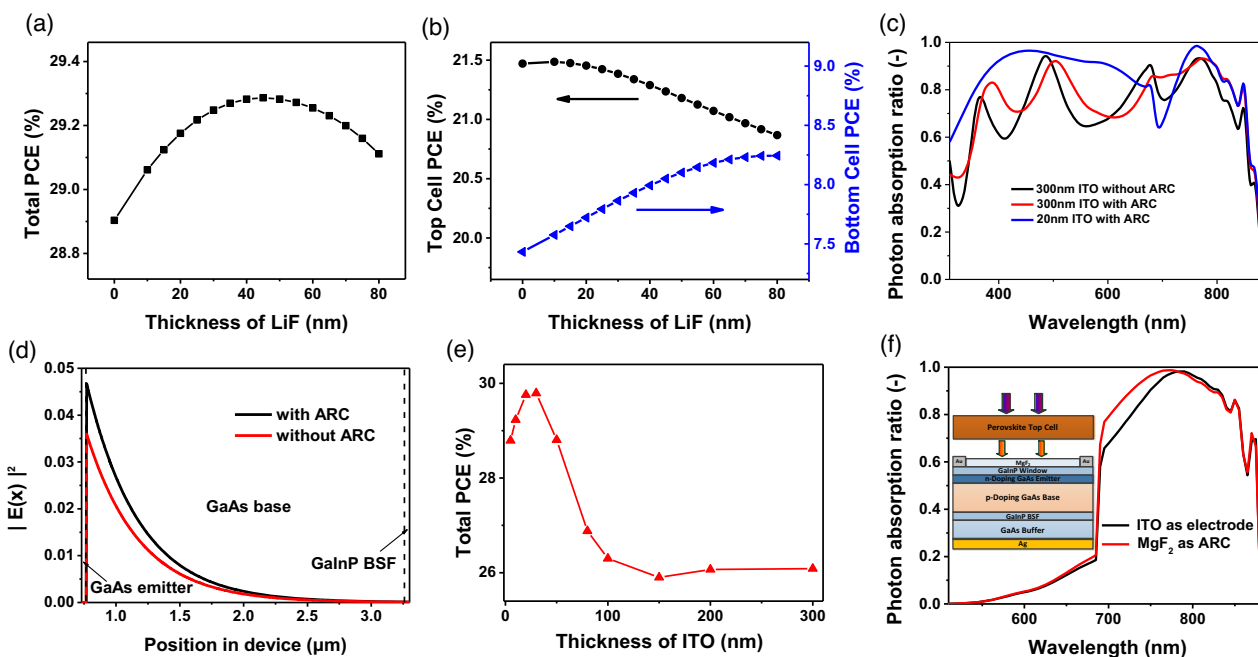
Figure 4. a) Total PCE of the device and b) PCEs of the subcells with different thicknesses of LiF. c) Photon absorption ratio under different conditions. d) Optical electric field ($|E(x)|^2$) of 700 nm wavelength. e) Total PCE of devices with different thicknesses of front ITO electrodes. f) Photon absorption of GaAs bottom cell with ITO or MgF$_2$.

shows that the introduction of the ARC has significantly improved the optical electric field of the GaAs bottom cell. Similarly, we speculate that reflections from the front ITO electrode can also reduce the photon absorption rate. As shown in Figure 4c, thinner ITO significantly increases the photon absorption in the wavelength range of 300–700 nm. It has almost no effect on absorption above 700 nm, which shows that ITO is more sensitive to short-wavelength light, and the reduction in thickness can increase the photon absorption of the top cell. According to the report of Consonni et al.,[45] a severe decrease in conductivity would happen when the ITO is very thin. As a result, the PCE decreases when the thickness of ITO is below 30 nm, as shown in Figure 4e. For the comprehensive consideration of conductivity and photon absorption rate, the maximum total efficiency can be achieved by setting the thickness of ITO to 30 nm. Furthermore, independent GaAs bottom cell can use ARC (MgF$_2$)[29,44] and metal electrode instead of ITO to achieve lower absorption loss, resulting in an improvement in the light absorption of 650–770 nm, as shown in Figure 4f. By introducing appropriate ARC and optimizing the thickness of the front ITO electrode, the total PCE of the 4-T perovskite/GaAs tandem solar cells increases from 28.90% to 29.91%.

2.1.4. Study of GaAs Base Doping

The doping concentration of GaAs base often affects the performance of GaAs tandem solar cells. When the concentration increases, as shown in **Figure 5**a, the bottom cell PCE tends to rise slowly and then decreases rapidly, reaching a maximum at a doping concentration of 10^{18} cm^{-3}. As shown in Figure 5b, the increase in the doping concentration of GaAs base causes J_{sc} to decrease continuously, and open-circuit voltage (V_{oc}) increases

first and tends to be saturated at 10^{19} cm^{-3}. To investigate the cause of this phenomenon, the recombination rate and energy band of GaAs bottom cell at different doping concentrations are investigated. Figure 5c shows that the increase in the GaAs base doping concentration would lead to a considerable increase of the recombination rate in GaAs base. Specifically, when the concentration reaches 10^{21} cm^{-3}, the recombination rate in GaAs base even remains above 10^{20} cm^{-3} s^{-1}. The increase in doping concentration introduces a mass of impurity defect recombination centers inside GaAs base, which causes the recombination rate to increase and J_{sc} to decrease. As shown in Figure 5d, the higher doping concentration results in a more bent energy band of the GaAs base, making V_{oc} improve to a certain extent. When the energy band bending reaches its limit, V_{oc} tends to be saturated. Therefore, considering the compromise between the recombination rate and the degree of band bending, 10^{18} cm^{-3} is selected as the GaAs doping concentration. This approach increases the total PCE of 4-T tandem solar cells from 29.91% to 30.97%. At the same time, the suitable doping concentration of GaAs base balances V_{oc} and J_{sc} of the bottom cell. Furthermore, it is of great significance to study the current matching and optimize the PCE of 2-T perovskite/GaAs tandem solar cells.

2.2. Simulation Results and Optimization of 2-T Configuration

The subcells of the 4-T tandem solar cells are structurally independent, and there is only an optical connection between them. In addition, the subcells each form an independent current path. For the 2-T configuration, due to its monolithic structure, the two subcells are connected by an intermediate layer, so the current of 2-T tandem solar cells is limited by the subcells with the smaller
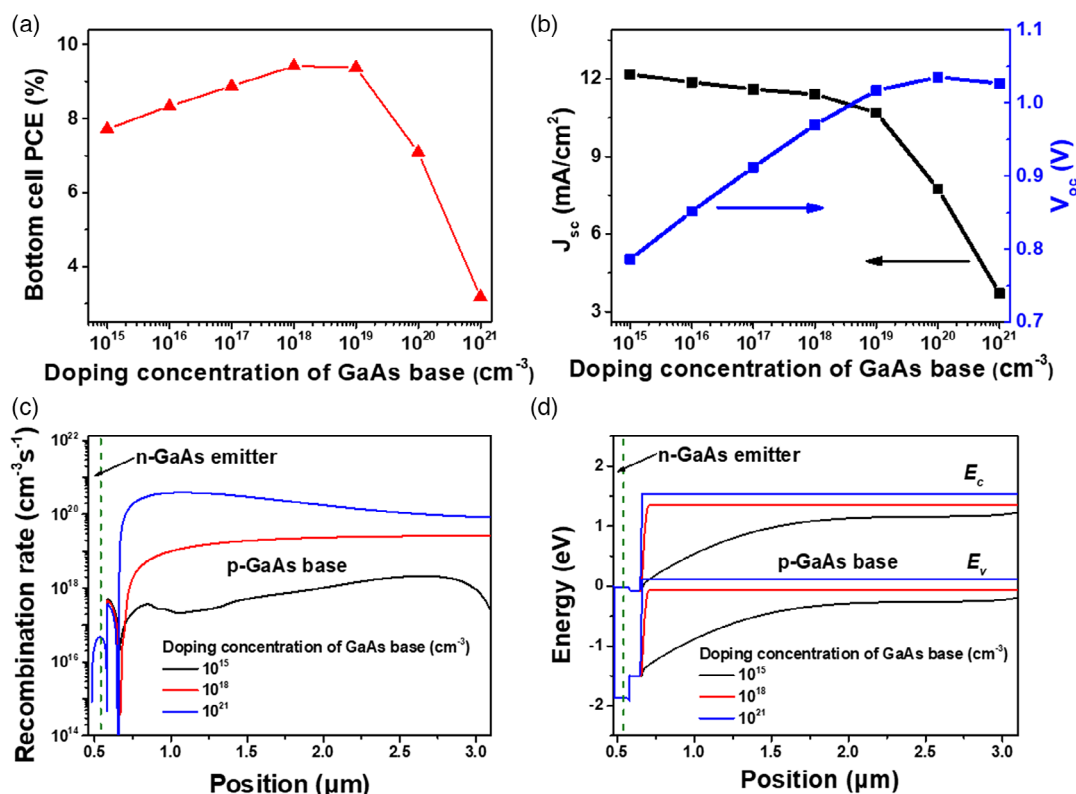
Figure 5. a) Bottom cell PCE and b) J_{sc} and V_{oc} as a function of doping concentration of GaAs base. c) Recombination rate and d) energy band diagrams in GaAs bottom cell with different doping concentrations of GaAs base.

current. The 2-T configuration has a wider range of commercial applications than the 4-T configuration. Therefore, current matching is extremely necessary in the design of 2-T configuration. Four kinds of all-inorganic perovskite materials ($CsPbI_3$, $CsPbI_2Br$, $CsPbIBr_2$, and $CsPbBr_3$) are selected as top cell perovskite absorption layers, respectively. The parameters of these all-inorganic perovskite materials are obtained from the literature.[37,39–41] When the thickness of perovskite increases within a certain range, the perovskite captures more photons, leading to the current of the top cell to rise continuously. At the same time, this also causes fewer photons to inject to the GaAs bottom cell, thereby reducing its current. When the thickness of the GaAs base increases within a certain range, the captured photons also increase, thereby improving the current of GaAs bottom cell. However, the current would reach saturation when the thickness increases to a certain extent. Therefore, the simulations of perovskite absorption layers and GaAs bases with different thicknesses are performed to find the current balanced points between the two subcells. It is of great significance to find the optimal PCE and maximize material savings. As exhibited in **Figure 6**, a current-matching point can be obtained at intersections of J_{sc} plane of the top cell and the bottom cell. A higher current-matching point means that a 2-T tandem solar cell can obtain a higher J_{sc} at this thickness. **Figure 7**a shows that with the Br component of inorganic perovskite $CsPbI_{3-x}Br_x$ ($3 \geq x \geq 0$) increases, its bandgap (E_g) also increases from 1.7 to 2.30 eV ($CsPbI_3$: 1.7 eV, $CsPbI_2Br$: 1.82 eV, $CsPbIBr_2$: 2.03 eV,

and $CsPbBr_3$: 2.3 eV),[37] which reduces optical absorption and matching J_{sc}. Finally, the current density–voltage (J–V) curves of the 2-T tandem solar cells composed of each all-inorganic perovskite $CsPbI_{3-x}Br_x$/GaAs with optimal performance are shown in Figure 7b (the detailed parameters are detailed in **Table 3**). According to the simulation results, the 2-T all-inorganic perovskite/GaAs tandem solar cells achieve the optimal PCE of 28.71% using $CsPbIBr_2$ as the top cell perovskite absorption layer, and the absorption profile is shown in Figure S4, Supporting Information.

To further optimize the efficiency of the 2-T $CsPbIBr_2$/GaAs tandem devices, the performance of different doping concentrations of GaAs base under optimal conditions is studied. As shown in Figure 7c, when the doping concentration reaches 10^{19} cm^{-3}, the PCE further increases to 30.67%, among which J_{sc} decreases to 13.03 mA cm^{-2}, and V_{oc} increases to 2.69 V. Remarkably, as the doping concentration of GaAs base increases, J_{sc} of 2-T tandem solar cells decreases and V_{oc} increases. This situation is consistent with the investigation of doping concentration in the study of 4-T GaAs bottom cell.

In experiments, the density of defects has a significant impact on the performance of tandem solar cells, and factors such as grain boundaries introduce defects to the perovskite film.[46] In this study, perovskite defect density is set to 10^{15} cm^{-3} initially. To study how perovskite defect density affects the performance of 2-T $CsPbIBr_2$/GaAs tandem solar cells, different defect densities are simulated, as shown in Figure 7d. The
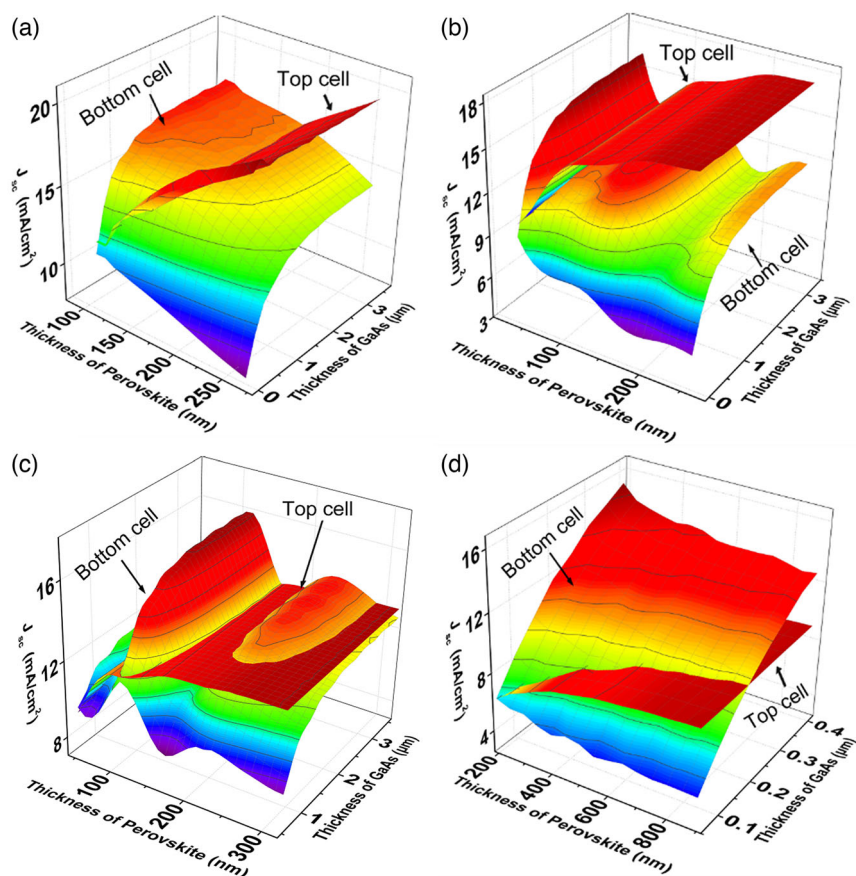
Figure 6. Current matching of 2-T a) $CsPbI_3$, b) $CsPbI_2Br$, c) $CsPbIBr_2$, and d) $CsPbBr_3$/GaAs tandem solar cells.
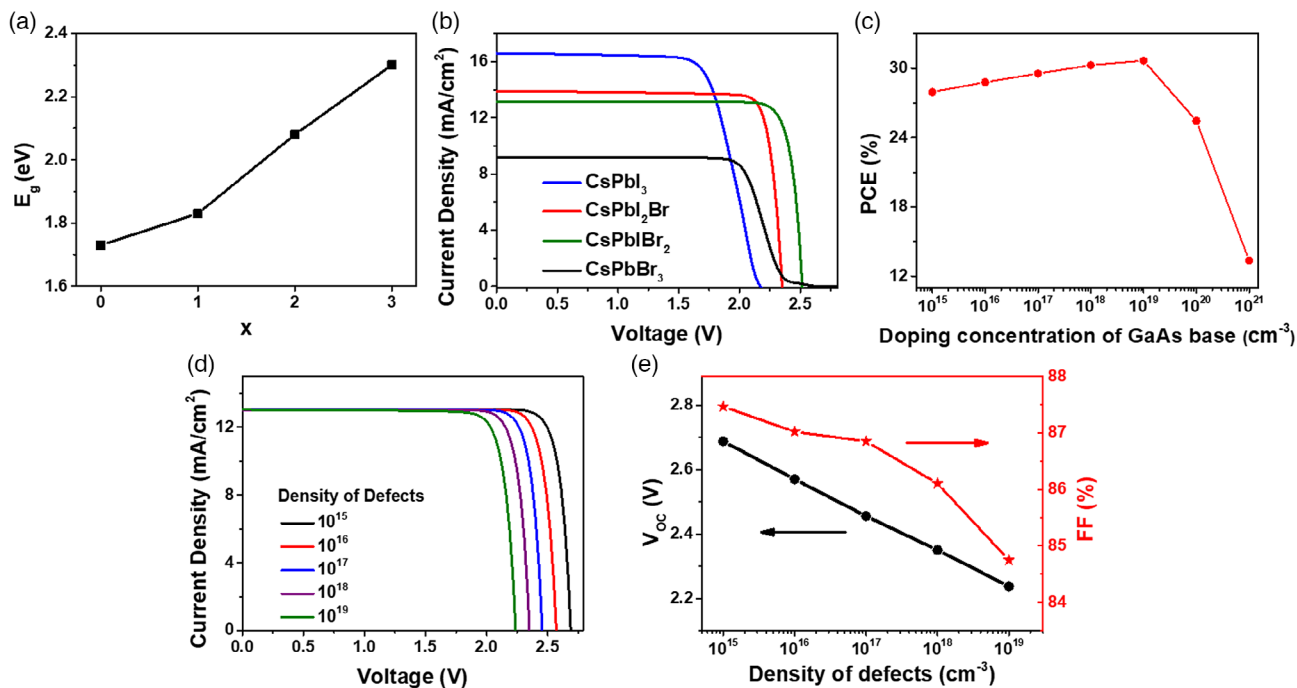
Figure 7. a) E_g of $CsPbI_{3-x}Br_x$ ($3 \geq x \geq 0$). b) $J-V$ curves of optimal 2-T $CsPbI_{3-x}Br_x$/GaAs tandem solar cells. c) PCEs of 2-T $CsPbIBr_2$/GaAs tandem solar cells with different doping concentrations of GaAs base. d) $J-V$ curves, and e) V_{oc} and FF of devices with different densities of defects.

Table 3. The best performance of 2-T $CsPbI_{3-x}Br_x$ /GaAs tandem solar cells at the points of current matching.

	J_{sc} [mA cm^{-2}]	V_{oc} [V]	FF [%]	PCE [%]
$CsPbI_3$	16.61	2.17	72.44	26.14
$CsPbI_2Br$	13.91	2.35	86.14	28.14
$CsPbIBr_2$	13.14	2.52	86.88	28.71
$CsPbBr_3$	9.17	2.78	68.07	17.38

increase in defects does not reduce J_{sc}, but V_{oc} and fill factor (FF) of 2-T tandem solar cells decrease significantly. Figure 7e shows that when the perovskite defect density increases from 10^{15} to 10^{19} cm^{-3}, a V_{oc} of the 2-T tandem device decreases from 2.69 to 2.24 V, and an FF decreases from 87.47% to 84.75%, which drastically reduces a PCE from 30.67% to 24.72%. The impairment of 2-T perovskite tandem solar cells performance by high perovskite defect density is obvious, so it should be reduced as much as possible in the experiment.

2.3. An Organic-Free 2-T Configuration for High Altitude/Space Applications

Considering the poor processing of organic HTLs in p-i-n perovskite top cell, the NiO film is used as inorganic HTL as well. In addition, it can avoid the organic component in the configuration to improve the stability of the device and can further meet the potential requirement of altitude/space application. The material parameters of NiO are obtained from the literature.[47]

First, 50 nm NiO with an N_A of 10^{20} cm^{-3} was introduced to 4-T all-inorganic $CsPbIBr_2$/GaAs tandem solar cells studied earlier to investigate its parasitic absorption. As shown in Figure S5, Supporting Information, the result tells its little parasitic absorption as organic HTL. Subsequently, current matching was performed on NiO-based $CsPbIBr_2$ and GaAs tandem devices, and the results are given in **Figure 8**a. At the points of current matching, the optimal PCE obtained 28.01%, and the details are shown in Figure S6, Supporting Information. Similarly, after adjusting the doping concentration of GaAs base in bottom cell, V_{oc} increases, whereas J_{sc} decreases, resulting in an optimized PCE of 29.42%, which is congruous to the organic HTL-based devices.

For traditional 2-T GaAs solar cells, it is necessary to explore their performance under the AM0 spectrum to achieve altitude/space application.[48,49] Therefore, the 2-T $CsPbIBr_2$/GaAs tandem device is also simulated under the AM0 spectrum.[43] The results show that the device has a larger J_{sc} of 14.81 mA cm^{-2} and a lower PCE of 25.99% than those of the AM1.5G spectrum, as shown in Figure 8e. The improvement of J_{sc} is due to the higher radiation intensity of the AM0 spectrum (1366.1 W m^{-2}) compared with the AM1.5G spectrum (1000 W m^{-2}).[43] The reason for the decrease in PCE is, on the one hand, the increase in spectral irradiance beyond the
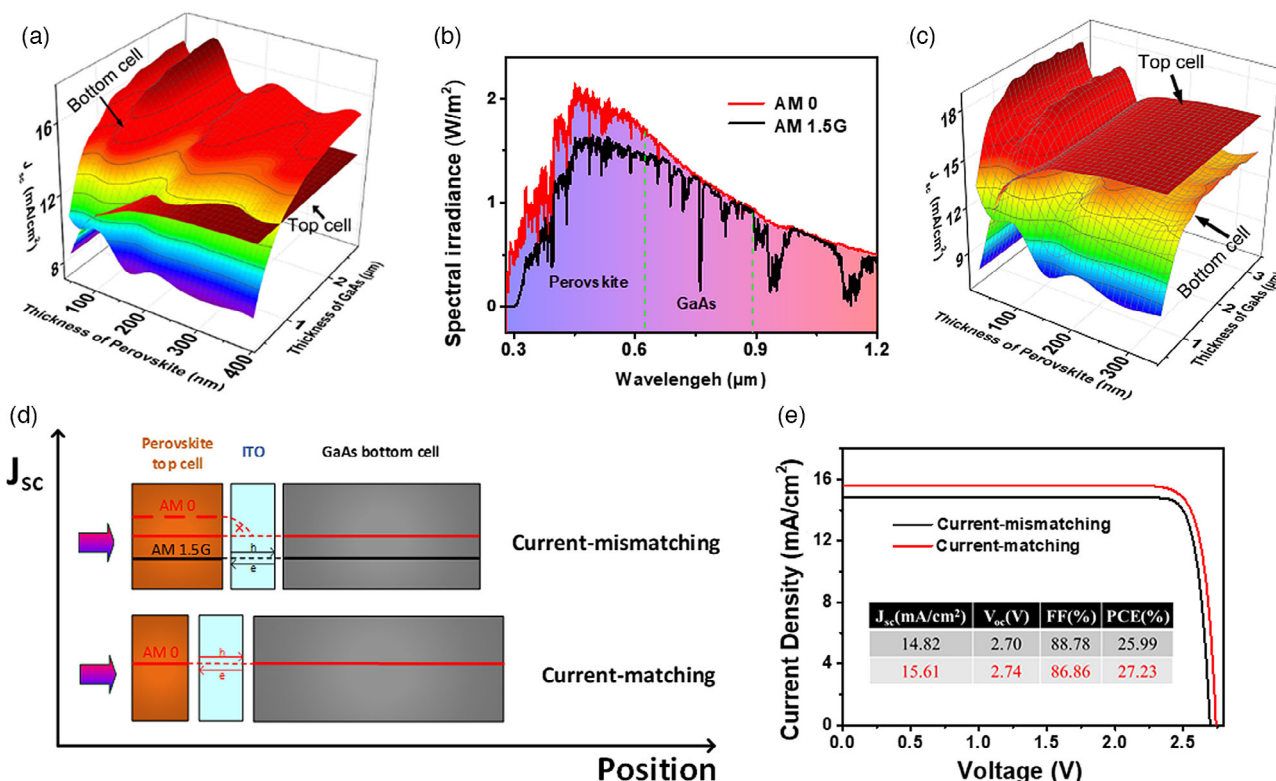
Figure 8. a) Current matching of 2-T $CsPbIBr_2$/GaAs tandem solar cells with NiO as HTL. b) Spectral irradiance of AM0 and AM1.5G solar spectra. c) Current matching of organics-free 2-T configuration under illumination of AM0 spectrum. d) Schematic diagram of current mismatching. e) J–V curves under illumination of AM0 spectrum.

absorption limit of the device. On the other hand, the increase of irradiance in the absorption range of GaAs is smaller than the increase of irradiance in the absorption range of $CsPbIBr_2$ (Figure 8b), so that the current mismatching between the subcells of the previous device is severe, as shown in Figure 8d. Therefore, it is essential to establish a new current matching under the AM0 spectrum to improve PCE for altitude/space application, as shown in Figure 8c. Obviously, the points of current matching under the AM0 spectrum move toward the thinner perovskite and the thicker GaAs base. As shown in Figure 8e, the optimal J–V curve of 2-T $CsPbIBr_2$/GaAs tandem solar cells under AM0 spectrum has a larger J_{sc} of 15.61 mA cm^{-2} compared with the previous mismatching current. Compared with the traditional GaAs double-junction tandem solar cell, it has a great competitive PCE of 27.23% with ARC and 26.21% without ARC (Table S1, Supporting Information).[48–51] Coupled with lower fabrication costs and simpler tunnel junctions, the 2-T all-inorganic $CsPbIBr_2$/GaAs tandem solar cells are of great potential for space or altitude application.

3. Conclusion

In this study, the planar structure 2-T and 4-T $CsPbI_{3−x}Br_x$/GaAs tandem solar cells are investigated. For 4-T configuration, the thicknesses of $CsPbI_2Br$, carrier transport layers, and GaAs base are optimized to minimize reflection loss and parasitic loss. To achieve a better PCE, ARC is introduced, and the front ITO electrode is studied. In addition, to balance J_{sc} and V_{oc} of GaAs bottom cell to achieve higher PCE, the doping concentration of GaAs base is selected as 10^{18} cm^{-3}. For 2-T configuration, the current matching is performed with all-inorganic perovskite $CsPbI_{3−x}Br_x$, and the doping concentration of GaAs base is optimized. Moreover, the effects of perovskite defect density are investigated as well. Perovskite defect density should be reduced as much as possible to increase V_{oc} and FF of 2-T tandem solar cells. Finally, an organic-free 2-T configuration is investigated by introducing NiO as inorganic HTL. The high PCEs of 29.42% under AM1.5G and 27.23% under AM0 are achieved based on organics-free 2-T $CsPbIBr_2$/GaAs tandem solar cells by eliminating current mismatching.

4. Experimental Section

In this study, Silvaco Technology Computer Aided Design (TCAD) is used as simulation platform, based on Poission's equation (Equation (1)), carrier continuity equation (Equation (2)), and drift–diffusion equation (Equation (3)).[41] As shown in Figure 1, a planar structure of ITO/ETL/perovskite/HTL/ITO is applied as perovskite top cell. According to Bertness's report,[50] a planar structure of ITO/GaInP window/n-GaAs emitter/p-GaAs base/GaInP back surface field (BSF)/GaAs buffer/Ag is applied as GaAs bottom cell. For 4-T configuration, a vacuum layer (5 nm) is inserted between the subcells. For 2-T configuration, the back electrode of the perovskite top cell and the front electrode of GaAs bottom cell are integrated as an ITO tunneling layer (5 nm). Shockley–Read–Hall (SRH) recombination, band-to-band recombination, and Auger recombination are considered as recombination models.[35,47] In addition, a transfer-matrix method is applied for calculating optical electric field to obtain carrier generation rate.[52] It is mainly based on Fresnel reflection and transmission principles to model interference phenomena caused by a large number of reflections in the interface of multilayer thin films.

Moreover, an AM1.5G global solar spectrum is used in this study. The perovskite density of defects is considered and set to the default of 10^{15} cm^{-3}.

$$\frac{\partial^2 \varphi}{\partial x^2} = \frac{q}{\varepsilon}(n-p) \tag{1}$$

$$\frac{\partial n}{\partial t} = \frac{1}{q}\frac{\partial J_n}{\partial x} + G - R \qquad \frac{\partial p}{\partial t} = -\frac{1}{q}\frac{\partial J_p}{\partial x} + G - R \tag{2}$$

$$J_n = qD_n\frac{\partial n}{\partial x} - q\mu_n n\frac{\partial \varphi}{\partial x} \qquad J_p = -qD_p\frac{\partial p}{\partial x} - q\mu_p p\frac{\partial \varphi}{\partial x} \tag{3}$$

Conflict of Interest

The authors declare no conflict of interest.

Data Availability Statement

Research data are not shared.

[1] A. Kojima, K. Teshima, Y. Shirai, T. Miyasaka, *J. Am. Chem. Soc.* **2009**, *131*, 6050.

[2] Z. Liu, J. Chang, Z. Lin, L. Zhou, Z. Yang, D. Chen, C. Zhang, S. F. Liu, Y. Hao, *Adv. Energy Mater.* **2018**, *8*, 1703432.

[3] L. Zhou, Z. Lin, Z. Ning, T. Li, X. Guo, J. Ma, J. Su, C. Zhang, J. Zhang, S. Liu, J. Chang, Y. Hao, *Sol. RRL* **2019**, *3*, 1900293.

[4] NREL, Best Research-Cell Efficiency Chart, https://www.nrel.gov/pv/cell-efficiency.html, **2020** (accessed: May 2020).

[5] S. Bai, P. Da, C. Li, Z. Wang, Z. Yuan, F. Fu, M. Kawecki, X. Liu, N. Sakai, J. T.-W. Wang, S. Huettner, S. Buecheler, M. Fahlman, F. Gao, H. J. Snaith, *Nature* **2019**, *571*, 245.

[6] J. Burschka, N. Pellet, S.-J. Moon, R. Humphry-Baker, P. Gao, M. K. Nazeeruddin, M. Grätzel, *Nature* **2013**, *499*, 316.

[7] S. D. Stranks, G. E. Eperon, G. Grancini, C. Menelaou, M. J. Alcocer, T. Leijtens, L. M. Herz, A. Petrozza, H. J. Snaith, *Science* **2013**, *342*, 341.

[8] Q. Zeng, X. Zhang, X. Feng, S. Lu, Z. Chen, X. Yong, S. A. T. Redfern, H. Wei, H. Wang, H. Shen, W. Zhang, W. Zheng, H. Zhang, J. S. Tse, B. Yang, *Adv. Mater.* **2018**, *30*, 1705393.

[9] B. Zhang, J. Su, X. Guo, L. Zhou, Z. Lin, L. Feng, J. Zhang, J. Chang, Y. Hao, *Adv. Sci.* **2020**, *7*, 1903044.

[10] J. Chang, H. Zhu, B. Li, F. H. Isikgor, Y. Hao, Q. Xu, J. Ouyang, *J. Mater. Chem. A.* **2016**, *4*, 887.

[11] J. Chang, Z. Lin, H. Zhu, F. H. Isikgor, Q.-H. Xu, C. Zhang, Y. Hao, J. Ouyang, *J. Mater. Chem. A.* **2016**, *4*, 16546.

[12] W. E. I. Sha, X. Ren, L. Chen, W. C. H. Choy, *Appl. Phys. Lett.* **2015**, *106*, 221104.

[13] Z. Hu, Z. Lin, J. Su, J. Zhang, J. Chang, Y. Hao, *Sol. RRL* **2019**, *3*, 1900304.

[14] C. D. Bailie, M. G. Christoforo, J. P. Mailoa, A. R. Bowring, E. L. Unger, W. H. Nguyen, J. Burschka, N. Pellet, J. Z. Lee, M. Grätzel, R. Noufi, T. Buonassisi, A. Salleo, M. D. McGehee, *Energy Environ. Sci.* **2015**, *8*, 956.

[15] Q. Han, Y. T. Hsieh, L. Meng, J. L. Wu, P. Sun, E. P. Yao, S. Y. Chang, S. H. Bae, T. Kato, V. Bermudez, Y. Yang, *Science* **2018**, *361*, 904.

[16] D. P. McMeekin, G. Sadoughi, W. Rehman, G. E. Eperon, M. Saliba, M. T. Horantner, A. Haghighirad, N. Sakai, L. Korte, B. Rech, M. B. Johnston, L. M. Herz, H. J. Snaith, *Science* **2016**, *351*, 151.

[17] P. Loper, S. J. Moon, S. M. de Nicolas, B. Niesen, M. Ledinsky, S. Nicolay, J. Bailat, J. H. Yum, S. De Wolf, C. Ballif, *Chem. Chem. Phys.* **2015**, *17*, 1619.

[18] J. H. Heo, S. H. Im, *Adv. Mater.* **2016**, *28*, 5121.

[19] P. Zhao, L. Feng, Z. Lin, J. Wang, J. Su, Z. Hu, J. Zhang, X. Ouyang, J. Chang, Y. Hao, *Sol. RRL* **2019**, *3*, 1900303.

[20] Q. Zeng, L. Liu, Z. Xiao, F. Liu, Y. Hua, Y. Yuan, L. Ding, *Sci. Bull.* **2019**, *64*, 885.

[21] M. Jošt, L. Kegelmann, L. Korte, S. Albrecht, *Adv. Energy Mater.* **2020**, *10*, 1904102.

[22] J. P. Mailoa, C. D. Bailie, E. C. Johlin, E. T. Hoke, A. J. Akey, W. H. Nguyen, M. D. McGehee, T. Buonassisi, *Appl. Phys. Lett.* **2015**, *106*, 121105.

[23] B. Chen, Z. J. Yu, S. Manzoor, S. Wang, W. Weigand, Z. Yu, G. Yang, Z. Ni, X. Dai, Z. C. Holman, J. Huang, *Joule* **2020**, *4*, 850.

[24] F. Sahli, J. Werner, B. A. Kamino, M. Brauninger, R. Monnard, B. Paviet-Salomon, L. Barraud, L. Ding, J. J. Diaz Leon, D. Sacchetto, G. Cattaneo, M. Despeisse, M. Boccard, S. Nicolay, Q. Jeangros, B. Niesen, C. Ballif, *Nat. Mater.* **2018**, *17*, 820.

[25] J. Zheng, H. Mehrvarz, F.-J. Ma, C. F. J. Lau, M. A. Green, S. Huang, A. W. Y. Ho-Baillie, *ACS Energy Lett.* **2018**, *3*, 2299.

[26] F. Sahli, B. A. Kamino, J. Werner, M. Bräuninger, B. Paviet-Salomon, L. Barraud, R. Monnard, J. P. Seif, A. Tomasi, Q. Jeangros, A. Hessler-Wyser, S. De Wolf, M. Despeisse, S. Nicolay, B. Niesen, C. Ballif, *Adv. Energy Mater.* **2018**, *8*, 1.

[27] I. Cardinaletti, T. Vangerven, S. Nagels, R. Cornelissen, D. Schreurs, J. Hruby, J. Vodnik, D. Devisscher, J. Kesters, J. D'Haen, A. Franquet, V. Spampinato, T. Conard, W. Maes, W. Deferme, J. V. Manca, *Sol. Energy Mater. Sol. Cells* **2018**, *182*, 121.

[28] J. Liang, C. Wang, Y. Wang, Z. Xu, Z. Lu, Y. Ma, H. Zhu, Y. Hu, C. Xiao, X. Yi, G. Zhu, H. Lv, L. Ma, T. Chen, Z. Tie, Z. Jin, J. Liu, *J. Am. Chem. Soc.* **2016**, *138*, 15829.

[29] Z. Li, T. H. Kim, S. Y. Han, Y. J. Yun, S. Jeong, B. Jo, S. A. Ok, W. Yim, S. H. Lee, K. Kim, S. Moon, J. Y. Park, T. K. Ahn, H. Shin, J. Lee, H. J. Park, *Adv. Energy Mater.* **2019**, *10*, 1903085.

[30] S. R. Kurtz, P. Faine, J. M. Olson, *J. Appl. Phys.* **1990**, *68*, 1890.

[31] Y. Han, H. Zhao, C. Duan, S. Yang, Z. Yang, Z. Liu, S. Liu, *Adv. Funct. Mater.* **2020**, *30*, 1909972.

[32] L. Zhou, X. Guo, Z. Lin, J. Ma, J. Su, Z. Hu, C. Zhang, S. Liu, J. Chang, Y. Hao, *Nano Energy* **2019**, *60*, 583.

[33] J. Ma, J. Su, Z. Lin, L. Zhou, J. He, J. Zhang, S. Liu, J. Chang, Y. Hao, *Nano Energy* **2020**, *67*, 104241.

[34] L. Zhou, J. Su, Z. Lin, X. Guo, J. Ma, L. Feng, J. Zhang, S. Wang, S. Liu, J. Chang, Y. Hao, *Sol. RRL* **2020**, *4*, 202000001.

[35] P. Zhao, Z. Lin, J. Wang, M. Yue, J. Su, J. Zhang, J. Chang, Y. Hao, *ACS Appl. Energy Mater.* **2019**, *2*, 4504.

[36] Q. Jiang, X. Zhang, J. You, *Small* **2018**, *14*, e1801154.

[37] P. Zhao, J. Su, Z. Lin, J. Wang, J. Zhang, Y. Hao, X. Ouyang, J. Chang, *Adv. Theory Simulations* **2020**, *3*, 2000055.

[38] T. Zhang, Y. Wang, X. Wang, M. Wu, W. Liu, Y. Zhao, *Sci. Bull.* **2019**, *64*, 1773.

[39] B. Yang, M. Wang, X. Hu, T. Zhou, Z. Zang, *Nano Energy* **2019**, *57*, 718.

[40] M. Zhao, Y. Shi, J. Dai, J. Lian, *J. Mater. Chem. C.* **2018**, *6*, 10450.

[41] M. Yue, J. Su, P. Zhao, Z. Lin, J. Zhang, J. Chang, Y. Hao, *Nano-Micro Lett.* **2019**, *11*, 91.

[42] P. Zhao, J. Su, Z. Lin, J. Wang, J. Zhang, Y. Hao, X. Ouyang, J. Chang, *Mater. Today Energy* **2020**, *17*, 100481.

[43] Atlas User's Guide, Silvaco, Santa Clara, CA **2016**.

[44] P. Zhao, Y. Hao, M. Yue, C. Lei, Z. Lin, J. Su, D. Chen, C. Zhang, J. Zhang, J. Chang, *IEEE J. Photovolt.* **2018**, *8*, 1685.

[45] V. Consonni, G. Rey, H. Roussel, B. Doisneau, E. Blanquet, D. Bellet, *Acta Mater.* **2013**, *61*, 22.

[46] T. S. Sherkar, C. Momblona, L. Gil-Escrig, J. Avila, M. Sessolo, H. J. Bolink, L. J. A. Koster, *ACS Energy Lett.* **2017**, *2*, 1214.

[47] P. Zhao, Z. Liu, Z. Lin, D. Chen, J. Su, C. Zhang, J. Zhang, J. Chang, Y. Hao, *Sol. Energy* **2018**, *169*, 11.

[48] T. Takamoto, E. Ikeda, H. Kurita, M. Ohmori, M. Yamaguchi, M. J. Yang, *Jpn. J. Appl. Phys.* **1997**, *36*, 6215.

[49] V. M. Lantratov, N. A. Kalyuzhnyĭ, S. A. Mintairov, N. K. Timoshina, M. Z. Shvarts, V. M. Andreev, *Semiconductors* **2007**, *41*, 727.

[50] K. A. Bertness, S. R. Kurtz, D. J. Friedman, A. E. Kibbler, C. Kramer, J. M. Olson, *Appl. Phys. Lett.* **1994**, *65*, 989.

[51] T. Takamoto, E. Ikeda, H. Kurita, M. Ohmori, *Appl. Phys. Lett.* **1997**, *70*, 381.

[52] Q. Lin, A. Armin, R. C. R. Nagiri, P. L. Burn, P. Meredith, *Nat. Photonics* **2014**, *9*, 106.

[53] Q. Zeng, X. Zhang, C. Liu, T. Feng, Z. Chen, W. Zhang, W. Zheng, H. Zhang, B. Yang, *Sol. RRL* **2019**, *3*, 1800239.

[54] R. Pandey, R. Chaujar, *J. Photonics Energy* **2017**, *7*, 022503.